



















RESEARCH ARTICLE | JUNE 12 2023

# Tuning terahertz emission generated by anomalous Nernst effect in ferromagnetic metal

Hui Zhang ; Zheng Feng ; Guansong Li ; Liang Zhang ; Xiaobing Chen ; He Bai ; Song Sun ; Jin Tang ; Jine Zhang ; Furong Han; Huaiwen Yang ; Wei Tan ; Yuansha Chen ; Fengxia Hu ; Jianwang Cai ; Liang Guo ; Sunmi Shin ; Weisheng Zhao ; Baogen Shen; Jirong Sun 



*Appl. Phys. Rev.* 10, 021417 (2023)

<https://doi.org/10.1063/5.0139197>



CrossMark

## AIP Advances

Why Publish With Us?



**25 DAYS**  
average time  
to 1st decision



**740+ DOWNLOADS**  
average per article



**INCLUSIVE**  
scope

[Learn More](#)



# Tuning terahertz emission generated by anomalous Nernst effect in ferromagnetic metal

Cite as: Appl. Phys. Rev. **10**, 021417 (2023); doi: [10.1063/5.0139197](https://doi.org/10.1063/5.0139197)

Submitted: 19 December 2022 · Accepted: 12 April 2023 ·

Published Online: 12 June 2023















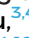






View Online



Export Citation



CrossMark

Hui Zhang,<sup>1,a)</sup>  Zheng Feng,<sup>2,a)</sup>  Guansong Li,<sup>3,4</sup>  Liang Zhang,<sup>5,6</sup>  Xiaobing Chen,<sup>7</sup>  He Bai,<sup>8</sup>  Song Sun,<sup>2</sup>  Jin Tang,<sup>9</sup>  Jine Zhang,<sup>1</sup>  Furong Han,<sup>1</sup>  Huaiwen Yang,<sup>1</sup>  Wei Tan,<sup>2</sup>  Yuansha Chen,<sup>3,4</sup>  Fengxia Hu,<sup>3,4,10</sup>  Jianwang Cai,<sup>3,4</sup>  Liang Guo,<sup>5</sup>  Sunmi Shin,<sup>6</sup>  Weisheng Zhao,<sup>1</sup>  Baogen Shen,<sup>3,4,11</sup> and Jirong Sun<sup>3,4,10,12,a)</sup> 

## AFFILIATIONS

<sup>1</sup>School of Integrated Circuit Science and Engineering, Beihang University, Beijing 100191, China

<sup>2</sup>Microsystem and Terahertz Research Center, CAEP, Chengdu, Sichuan 610200, China

<sup>3</sup>Beijing National Laboratory for Condensed Matter Physics and Institute of Physics, Chinese Academy of Sciences, Beijing 100190, China

<sup>4</sup>School of Physical Sciences, University of Chinese Academy of Sciences, Beijing 100049, China

<sup>5</sup>Department of Mechanical and Energy Engineering, Southern University of Science and Technology, Shenzhen 518055, China

<sup>6</sup>Department of Mechanical Engineering, National University of Singapore, Singapore 117576, Singapore

<sup>7</sup>Shenzhen Institute for Quantum Science and Engineering (SIQSE) and Department of Physics, Southern University of Science and Technology, Shenzhen 518055, China

<sup>8</sup>Spallation Neutron Source Science Center, Dongguan, Guangdong 523803, China

<sup>9</sup>School of Physics and Optoelectronics Engineering Science, Anhui University, Hefei 230601, China

<sup>10</sup>Songshan Lake Materials Laboratory, Dongguan, Guangdong 523808, China

<sup>11</sup>Ningbo Institute of Materials Technology and Engineering, Chinese Academy of Sciences, Ningbo, Zhejiang 315201, China

<sup>12</sup>Spintronics Institute, University of Jinan, Jinan, Shandong 250022, China

<sup>a)</sup>Authors to whom correspondence should be addressed: [huizh@buaa.edu.cn](mailto:huizh@buaa.edu.cn); [fengzheng\\_mtrc@caep.cn](mailto:fengzheng_mtrc@caep.cn); and [jrsun@iphy.ac.cn](mailto:jrsun@iphy.ac.cn)

## ABSTRACT

Despite intensive research, the mechanism determining the terahertz (THz) emission of the ferromagnetic (FM) metallic monolayers remains elusive. Here, we report on the results of a systematic investigation on the THz emission generated by pumping  $\text{Ni}_{80}\text{Fe}_{20}$  monolayers on  $\text{Al}_2\text{O}_3$  substrates with a femtosecond laser. We found solid evidence that the THz emission is dominated by the anomalous Nernst effect (ANE), in which a transient spin-polarized charge current can be induced by an ultrafast electron temperature gradient on the picosecond timescale, out-putting THz emission. We found a polarity reversal of the THz waveform after the introduction of a  $\text{SiO}_2$  buffer layer to the sample and found that, based on ultrafast temperature simulation, it was a consequence of direction reversal of temperature gradient. Comparing the THz emission of different FM monolayers further confirms that the THz polarity also strongly depends on the sign of the ANE coefficient. These phenomena unambiguously indicate that the ANE plays a decisive role in the process of THz emission. The present work shows the importance of ultrafast spin caloritronics for a spintronic THz emitter. The principle demonstrated here can be applied to other FM metallic materials.

Published under an exclusive license by AIP Publishing. <https://doi.org/10.1063/5.0139197>

## I. INTRODUCTION

The spintronic terahertz (THz) emitter based on spin-to-charge conversion has received a wide attention recently, due to its broad spectrum, low cost, and flexibility.<sup>1–5</sup> The typical spintronic THz emitter is a bilayer formed by a ferromagnetic (FM) metal and a

nonmagnetic (NM) metal with a strong spin-orbit coupling. In the FM layer, sub-picosecond spin-polarized electric current pulses can be generated by femtosecond (fs) laser excitation. When diffusing into the NM layer, they are converted into transient transverse charge currents by inverse spin Hall effect (ISHE) or inverse Rashba-Edelstein

effect (IREE),<sup>6,7</sup> outputting THz waves with the polarity state that is magnetically controllable.

In addition to the works on FM/NM bilayer-typed THz emitters, there are also reports on the THz emission from a FM metallic monolayer.<sup>8–20</sup> The first report was given by Beaurepaire *et al.* in 2004.<sup>8</sup> In that work, THz emissions from a 42-Å-thick Ni film were observed and were ascribed to magnetic dipolar radiation caused by ultrafast demagnetization.<sup>8,21–24</sup> Although magnetic dipole radiation only produces very weak THz emission, the information from the THz spectrum is important for revealing the ultrafast spin dynamics and ultrafast spin-transport processes in the FM film and FM film-based heterostructures.<sup>15–19,25</sup> The explanation that ultrafast demagnetization yields THz emission has seldom been challenged for a long time. Recently, however, THz polarity reversal was observed when changing the pumping side from the substrate to film by flipping the FM sample (magnetization direction keeps unchanged).<sup>26,27</sup> This is in contradiction to the features of the THz waves yielded by ultrafast demagnetization, which is expected to be unaffected by sample flipping.<sup>13,15</sup> An alternative mechanism was proposed for this THz emission: In the substrate/ferromagnet/dielectric structure, the backflow current formed by the reflection of laser-excited hot electrons from the ferromagnet/dielectric interface can be converted into a transverse transient charge current by an anomalous Hall effect (AHE), producing THz waves.<sup>26</sup>

Recently, it is found that fs-laser-induced ultrafast thermal effects could also result in THz emission. When exciting the YIG/Pt bilayer, a prototypical structure of FM insulator/NM metal, with a fs laser pulse, an ultrafast spin current stemming from the spin Seebeck effect is produced by temperature gradient and then is converted into a transverse charge current by ISHE, emitting a THz wave pulse.<sup>28</sup> THz emission generated from the transient photothermoelectric current, induced by photo-Seebeck effect and photo-Nernst effect, has also been reported for a Dirac semimetal Cd<sub>3</sub>As<sub>2</sub>.<sup>29</sup> Specifically, the anomalous Nernst effect (ANE), a traditional magneto-thermal effect, was found to play an important role in generating THz emission from a FM metallic monolayer,<sup>30</sup> in addition to ultrafast demagnetization and AHE. Clearly, the mechanism determining the THz emission of the FM single layer remains elusive and warrants further investigations.

In this work, we performed a systematic investigation on THz emission from the Ni<sub>80</sub>Fe<sub>20</sub> (NiFe) films on Al<sub>2</sub>O<sub>3</sub> substrates, produced by ultrafast laser pumping. To tune the laser-pulse-induced temperature gradient in the sample, we introduced a buffer layer of SiO<sub>2</sub>, a thermal insulator, and compared the THz emissions from the buffered and non-buffered samples. The most remarkable observation is a 180° phase change in the THz waveforms after the introduction of the buffer layer, a phenomenon that cannot be explained by either ultrafast demagnetization or AHE effect. We found conclusive evidence that the THz emission mainly stems from ANE, in which an ultrafast electron temperature gradient on picosecond timescale can induce a transient spin-polarized charge current, yielding THz emission. There are signatures that the ANE is composed of interface and bulk components, and the interface temperature gradient can be effectively tuned by the buffer layer. Moreover, by comparing the THz emission of Fe, Co, and NiFe monolayers, we found that the decisive factor leading to the polarity reversal of the THz waveform is the sign of the ANE coefficient, not the AHE coefficient, thus excluding the contribution of the AHE of hot electrons. The present work verifies

the mechanism of ANE-induced THz emission from a new perspective and provides flexible methods to tune THz emission.

## II. RESULTS AND DISCUSSION

### A. Tuning THz emission from ferromagnetic metal via interface engineering

The experiment setup for THz emission spectroscopy is schematically shown in Fig. 1(a). A linearly polarized fs laser pulse with a power of 900 mW is incident to the sample along the *z* axis; then, a THz signal with an electric field along *x* axis is emitted when a magnetic field (*H*) is applied along *y* axis (0.1 T). Figure 1(b) shows the typical THz temporal waveforms from a 5-nm-thick Ni<sub>80</sub>Fe<sub>20</sub> (NiFe) film without or with a 3-nm-thick SiO<sub>2</sub> buffer layer, obtained by pumping substrate side. We observed obvious THz emission from Al<sub>2</sub>O<sub>3</sub>/NiFe(5 nm)/SiO<sub>2</sub>(3 nm) when the sample suffers from the stimuli of ultrafast laser pulse, here SiO<sub>2</sub> is a cap layer protecting NiFe from oxidization. For the THz emitter Al<sub>2</sub>O<sub>3</sub>/SiO<sub>2</sub>(3 nm)/NiFe(5 nm)/SiO<sub>2</sub>(3 nm), surprisingly, not only the intensity of the THz emission is enhanced but also the polarity of the THz waveform is reversed.

For a single FM layer, in general, the laser induced ultrafast demagnetization of NiFe results in the emission of a THz pulse proportional to the second time derivative of the magnetization  $d^2M/dt^2$ , which can be explained by the radiation from a time-dependent magnetic dipole described by Maxwell's electromagnetism theory.<sup>8</sup> According to the electromagnetism theory, magnetic dipole radiation is determined by magnetization dynamics. Since inserting a buffer layer does not change the ultrafast demagnetization process of the FM layer, the polarity of the THz waveforms is expected to be unaffected. The AHE mechanism cannot explain experiment results either. As declared, the laser excited hot electrons in the ferromagnet will induce backflow superdiffusion currents at the FM/dielectric interfaces.<sup>26</sup> For Al<sub>2</sub>O<sub>3</sub>/NiFe(5 nm)/SiO<sub>2</sub>(3 nm), the top and bottom interfaces of NiFe are asymmetric so that the backflow currents from the two interfaces may not be canceled out and form a net backflow current, which is then converted into a transverse transient charge current by the AHE and emits terahertz waves. Obviously, the net backflow current is closely related to two interfaces, i.e., the THz emission will strongly depend on the Al<sub>2</sub>O<sub>3</sub>/NiFe and NiFe/SiO<sub>2</sub> interfaces. Inserting a thin SiO<sub>2</sub> buffer layer between the NiFe and Al<sub>2</sub>O<sub>3</sub> will considerably eliminate interface asymmetry. It should be noted that even in the case of symmetric interfaces, i.e., SiO<sub>2</sub>/NiFe/SiO<sub>2</sub>, the roughness of the bottom interface and the upper interface is difficult to be exactly the same, which makes the net backflow current unable to be fully compensated. Therefore, the THz radiation originating from AHE may also occur in Al<sub>2</sub>O<sub>3</sub>/SiO<sub>2</sub>(3 nm)/NiFe(5 nm)/SiO<sub>2</sub>(3 nm). However, the same type of the NiFe/dielectric interfaces would result in a smaller net backflow current, which significantly depresses the THz emission. This is inconsistent with the experimental results. As shown in Fig. 1(b), the intensity of the THz wave enhances after inserting a buffer layer. Moreover, the AHE mechanism fails to explain the polarity reversal of the THz waveform. Therefore, an additional mechanism should exist, responsible for the anomalous THz emission.

The anomalous Nernst effect (ANE) is the thermal counterpart of AHE. The ANE in ferromagnetic metals can generate a spin-polarized current.<sup>31–35</sup> A temperature gradient ( $\nabla T$ ) in a ferromagnetic metal causes a splitting between spin-up and spin-down chemical potentials, owing to the spin-dependent density of states.<sup>36</sup>

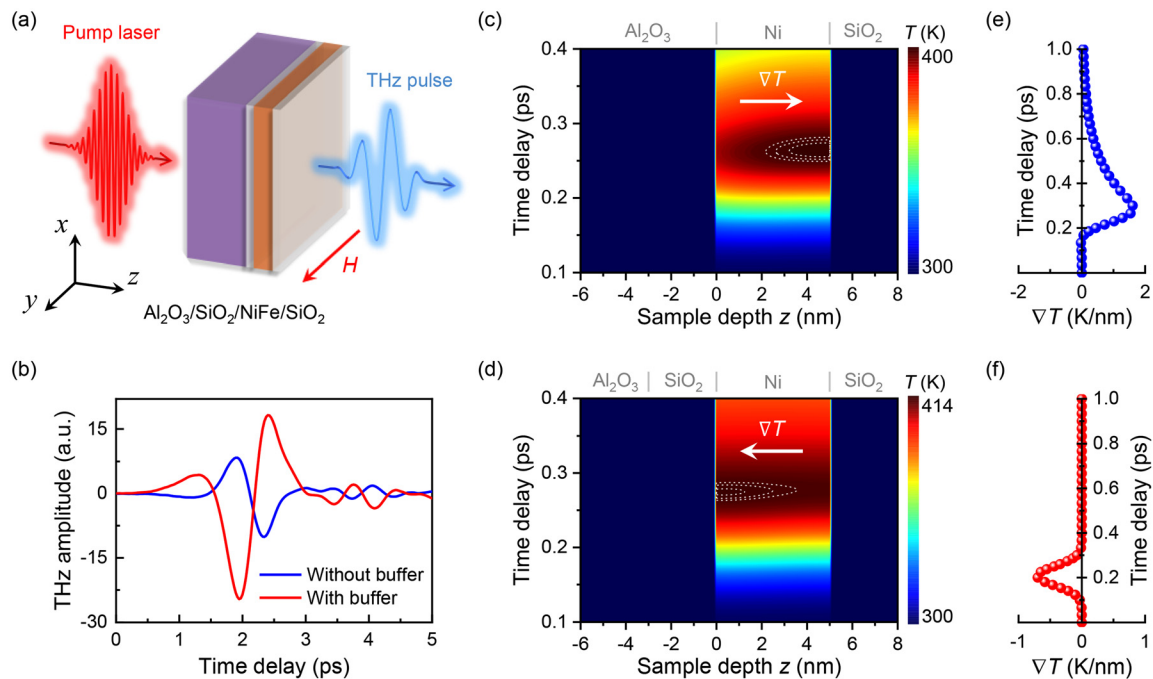


**FIG. 1.** (a) A sketch for the experimental generation of THz emissions. (b) Typical temporal THz waveforms from a 5-nm-NiFe single layer grown on the  $\text{Al}_2\text{O}_3$  substrate, without and with a 3-nm-thick  $\text{SiO}_2$  buffer layer. (c) and (d) Two-dimensional color maps of temperature distribution in  $\text{Al}_2\text{O}_3/\text{Ni}(5\text{ nm})/\text{SiO}_2(3\text{ nm})$  (c) and  $\text{Al}_2\text{O}_3/\text{SiO}_2(3\text{ nm})/\text{Ni}(5\text{ nm})/\text{SiO}_2(3\text{ nm})$  (d), obtained by ultrafast temperature simulation while pumping substrate side with an incident fluence of  $0.7\text{ J}\cdot\text{m}^{-2}$ . The sample depth  $z$  is the distance from the left side of the Ni film. For clarity, the white dashed lines are used to mark the high temperature center of the isotherm. (e) and (f) The corresponding transient temperature gradients in the Ni layer. Here, the thermophysical parameters of Ni were adopted since they are difficult to be obtained from the literature for NiFe. This will not affect the final conclusion because of the similarity of NiFe and Ni.

An electromotive force  $E_{\text{ANE}} = -\alpha\mathbf{m} \times \nabla T$  emerges along the direction perpendicular to both the magnetization and the temperature gradient, where  $\alpha$  is the ANE coefficient and  $\mathbf{m}$  is the unit vector of magnetization.<sup>31</sup> Thus, the spin-polarized current can be driven by a temperature gradient via ANE. In our experimental configuration, when the fs laser pulse is incident onto the sample along the  $z$ -axis, as shown in Fig. 1(a), a transient temperature gradient  $\nabla T$  along  $z$  axis will be established in the FM metal by the effect of laser heating, and then the spin separation of the charge carriers in the FM layer via ANE will cause a transient spin-polarized charge current  $J_c \propto E_{\text{ANE}} = -\alpha\mathbf{m} \times \nabla T$ ,<sup>35,37</sup> where  $\mathbf{m}$  is parallel to the external magnetic field along  $y$  axis,  $J_c$  flows along  $x$  axis and generates a THz emission along  $z$  axis. According to this mechanism, when the direction of  $\mathbf{m}$  is reversed by applying field the direction of  $J_c$  will be reversed simultaneously, leading to a  $180^\circ$  phase change in the THz waveform. Alternatively, changing the direction of the temperature gradient in the FM layer will also cause a polarity reversal of the THz waveform. In order to confirm that the generated charge current follows the above relationship with magnetization, the THz emissions of  $\text{Al}_2\text{O}_3/\text{NiFe}(5\text{ nm})/\text{SiO}_2(3\text{ nm})$  and  $\text{Al}_2\text{O}_3/\text{SiO}_2(3\text{ nm})/\text{NiFe}(5\text{ nm})/\text{SiO}_2(3\text{ nm})$  under opposite magnetic field directions were measured. We found that rotating the direction of magnetization within the  $xy$  plane by reversing the magnetic field direction from the  $+y$  axis to the  $-y$  axis results in a  $180^\circ$  phase change in the THz waveform (see Fig. S1 of the [supplementary material](#)), indicating that the direction of the electric field of the THz signal is reversed, which is consistent with the ANE mechanism for THz

generation. In the following discussion, we will fix the external magnetic field along the  $+y$  axis, focusing on the influence of the temperature gradient.

In static measurements, the electron temperature and lattice temperature are the same. However, they are different in the ultrafast process. When an ultrafast laser beam is focused on a metal, the photon energy is first absorbed by free electrons, and it takes a few tens to a few hundreds of femtoseconds for the electrons to reach thermal equilibrium. The electron-phonon coupling will also heat up the metal lattice. However, the energy transfer from electrons to lattice in metal take a time longer than picosecond to finish, a typical timescale for THz emission. Therefore, the ANE that induces the THz emission from the FM monolayer is caused by the temperature gradient of the electrons in the ultrafast process, rather than by the temperature gradient of the lattice. For thin metal films on a dielectric substrate, there can be an electron-phonon coupling across the substrate/metal interface as well, which spreads the energy into the substrate through heat diffusion. Notably, the timescale of this coupling between metal electrons and substrate phonons can be less than 1 ps, shorter than that of the electron-phonon coupling in metal.<sup>38–40</sup> Therefore, the metal electron temperature near the substrate/metal interface will be lower than that away from interface in the timescale shorter than 1 ps (in the condition of the uniform laser energy absorption), due to the ultrafast energy transfer from metal electrons to substrate phonons. In other words, an ultrafast electron temperature gradient with the timescale shorter than 1 ps will be established upon fs laser illumination, even in

a very thin FM film. After introducing an oxide insulator buffer layer between FM metal and substrate, the coupling between metal electrons and substrate phonons becomes the coupling between metal electrons and buffer layer phonons, which will change the ultrafast temperature distribution of electrons in the FM metal and even reverse the ultrafast electron temperature gradient. If not particularly emphasized, hereafter the temperature gradient will refer to the electron temperature gradient in the FM monolayer.

To quantitatively analyze the temperature gradient in the FM layer, we carried out ultrafast temperature simulations using a one-dimensional two temperature model (TTM).<sup>39</sup> The detailed simulation model is presented in Methods. Here, the thermophysical parameters of Ni were adopted<sup>21</sup> since they are difficult to be obtained from the literature for NiFe. This will not affect the final conclusion because of the similarity of NiFe and Ni. During the simulation, the thickness is set to 10 nm for the Al<sub>2</sub>O<sub>3</sub> substrate and to 5 nm for the Ni layer. Pumping the substrate side with an incident fluence of 0.7 J·m<sup>-2</sup>, the spatial-temporal temperature maps  $T(z, t)$  are obtained and shown in Figs. 1(c) and 1(d) for the samples without and with a buffer layer. For clarity, white dashed lines are used to mark the high temperature center of the isotherm. The corresponding spatial-temporal phonon temperature maps are shown in Fig. S2 of the [supplementary material](#). The heating effect of the laser illumination on metal is especially strong, and the laser absorption is much greater for the Ni layer than for the Al<sub>2</sub>O<sub>3</sub> substrate and the SiO<sub>2</sub> layer, regardless of whether the buffer layer exists or not. Thus, temperature changes have taken place

in the Ni layer. The corresponding transient temperature gradient in the Ni layer is depicted in Fig. 1(e) (without buffer layer) and Fig. 1(f) (with a SiO<sub>2</sub> buffer layer). We found that the direction of the temperature gradient is reversed after the introduction of a buffer layer, although the magnitude of the temperature gradient does not increase after inverse. For the sample without a buffer layer, due to the thermal conduction through the much thicker substrate, a temperature gradient is established in the FM layer along  $+z$  axis (from substrate to FM layer); thus, the sign of  $\nabla T$  is positive as shown in Fig. 1(e). At room temperature, the thermal conductivity of SiO<sub>2</sub> is  $\sim 1.34 \text{ W}\cdot\text{m}^{-1}\cdot\text{K}^{-1}$ , which is nearly an order of magnitude smaller than that of the Al<sub>2</sub>O<sub>3</sub> substrate ( $\sim 36.69 \text{ W}\cdot\text{m}^{-1}\cdot\text{K}^{-1}$ ).<sup>41,42</sup> Therefore, the SiO<sub>2</sub> buffer layer is a good thermal insulator. It eliminates the thermal exchange between FM layer and substrate. As a result, a  $\nabla T$  along  $-z$  axis establishes, i.e., for the sample with a SiO<sub>2</sub> buffer layer, a negative  $\nabla T$  is obtained, as shown in Fig. 1(f). The simulation results provide a good interpretation for the polarity reversal after the introduction of a buffer layer in Fig. 1(c). In addition, we extract the THz electric field generated by ANE under the temperature gradient obtained in Fig. 1(e) (see Note 1 and Fig. S3 of the [supplementary material](#)) and obtain a THz electric field amplitude of about 17.6 V/cm, which is large enough for experimental measurements.

We further investigate the influence of the thickness of the buffer layer on THz emission. THz signals are shown in Fig. 2(a) for the sample of Al<sub>2</sub>O<sub>3</sub>/SiO<sub>2</sub>( $t_{\text{Buffer}}$ )/NiFe(5 nm)/SiO<sub>2</sub>(3 nm) with the buffer layer thickness ranging from  $t_{\text{Buffer}} = 0$  to 50 nm. We found polarity reversal

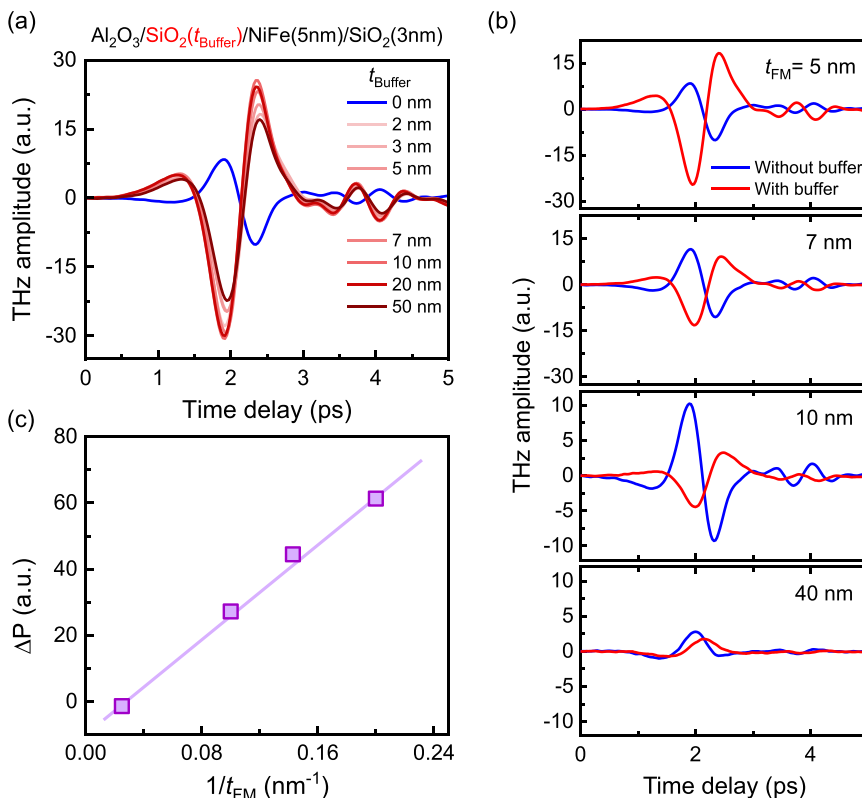


**FIG. 2.** (a) THz waveforms of the Al<sub>2</sub>O<sub>3</sub>/SiO<sub>2</sub>( $t_{\text{Buffer}}$ )/NiFe(5 nm)/SiO<sub>2</sub>(3 nm) samples for  $t_{\text{Buffer}}=0, 2, 3, 5, 7, 10, 20,$  and 50 nm. (b) THz waveforms emitted from the NiFe layers of different thickness ( $t_{\text{FM}}=5, 7, 10,$  and 40 nm). Both data without and with a 3 nm-thick buffer layer are shown. (c) Difference of the peak amplitudes of the THz signals without and with a buffer layer as a function of the inverse thickness of the FM layer. Solid line is a guide for the eye.



of the THz waveform for all samples with a buffer layer, i.e., whether polarity reversal takes place depends on whether the SiO<sub>2</sub> buffer layer is introduced, regardless of layer thickness. This result provides further evidence that the THz emission from the NiFe monolayer is dominated by ANE. As for the slight change in the intensity of the THz radiation with  $t_{\text{Buffer}}$ , it could be ascribed to the variation of the temperature gradient in magnitude.

In further research, we fixed the thickness of the buffer layer to 3 nm and set the thickness of the NiFe layer to  $t_{\text{FM}} = 5, 7, 10,$  and 40 nm. Figure 2(b) shows the THz waveforms of the samples with different NiFe layers. For comparison, the results of the corresponding samples without a buffer layer are also presented. Comparing with that without the buffer layer, the THz intensity is enhanced by buffer layer when  $t_{\text{FM}} = 5$  nm, unchanged when  $t_{\text{FM}} = 7$  nm, and reduced when  $t_{\text{FM}} = 10$  nm. When the FM layer is thick enough ( $t_{\text{FM}} = 40$  nm), the THz emission is very weak, and the effect of the buffer layer is unidentifiable. As a quantitative measure of the THz signals, the peak amplitude of the THz wave is defined by the difference between the first and the second extremes at 1.9 ps and 2.4 ps, respectively. The sign of this difference represents the polarity of the THz emission. The difference of the peak amplitude ( $\Delta P$ ) of the samples without and with a buffer layer provides a quantitative description for the tuning effect of the buffer layer. Figure 2(c) shows  $\Delta P$  as a function of the inverse thickness of the FM layer.  $\Delta P$  linearly grows as  $1/t_{\text{FM}}$  increases, i.e., the temperature gradient in the FM layer has been strongly modulated by the buffer layer. Notably, this linear relation is a fingerprint of the interfacial effect, as will be explained later.

## B. Thickness dependence of THz emission on a ferromagnetic metallic film

To confirm the ANE mechanism for THz generation, the THz emission is further studied for the Al<sub>2</sub>O<sub>3</sub>/NiFe( $t_{\text{FM}}$ )/SiO<sub>2</sub>(3 nm) samples with a  $t_{\text{FM}}$  ranging from 3 to 70 nm. As shown in Fig. 3(a), the THz waveforms exhibit a strong dependence on the layer thickness of NiFe and pumping side. THz emissions excited from the substrate side and the film side are measured by flipping samples. As a function of  $t_{\text{FM}}$ , the peak amplitudes, defined as the difference between the first and the second extremes of the THz waveforms, are presented in Fig. 3(b), where the magnitude and sign of the peak amplitude represent the intensity and the polarity of the THz waveforms, respectively. In the case pumping substrate, with the increase in  $t_{\text{FM}}$ , the THz peak amplitude first grows rapidly and then, when  $t_{\text{FM}}$  exceeds 7 nm, decreases steadily. When  $t_{\text{FM}} > 20$  nm, the sign of the peak amplitude undergoes a positive to negative transition, manifesting the polarity reversal of the THz waveforms. For clarity, in Fig. 3(a), we present the THz waveforms for  $t_{\text{FM}} = 3$  nm and 40 nm in the same plot to highlight polarity reversal in thick samples. When the film side is pumped, the magnitude of THz peak amplitude exhibits the same trend, first increasing and then decreasing with the increase in  $t_{\text{FM}}$ . However, the sign of the THz peak amplitude is always negative. Moreover, we also found that flipping sample causes the reversal of the THz polarity for thin FM layer samples ( $t_{\text{FM}} < 20$  nm). For thick FM layers ( $t_{\text{FM}} > 20$  nm), in contrast, the polarity of the THz waveforms is irrelevant to sample flipping, and the sign of the peak amplitude remains negative, regardless of which side is pumped.

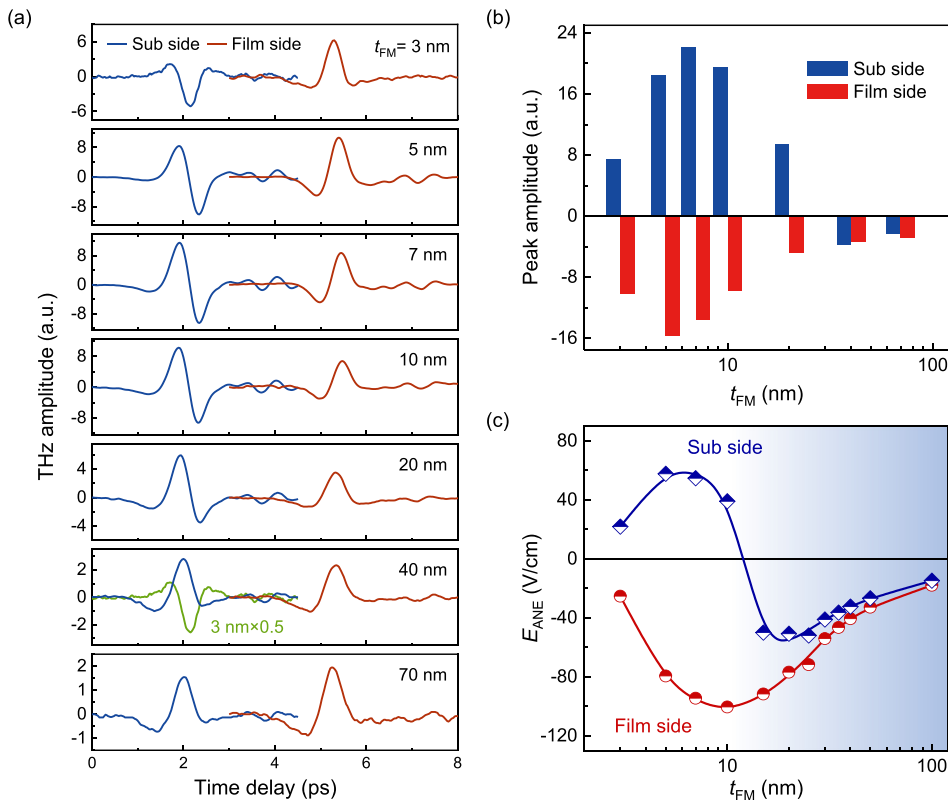


**FIG. 3.** (a) THz waveforms of the Al<sub>2</sub>O<sub>3</sub>/NiFe( $t_{\text{FM}}$ )/SiO<sub>2</sub>(3 nm) samples with  $t_{\text{FM}} = 3, 5, 7, 10, 20, 40,$  and 70 nm for substrate side and film side pumping. Data of 3 nm are also presented in the plot of 40 nm for comparison. (b) Dependence of the peak amplitude of THz signals in (a) on the FM layer thickness. For clarity, the red bars have been slightly moved to the right. (c) ANE electric field as a function of FM layer thickness, calculated by the equation  $E_{\text{ANE}} = -\alpha \mathbf{m} \times \nabla T$ , where  $\nabla T$  is obtained by ultrafast temperature simulation. Solid lines are guides for the eye.

As mentioned earlier, the anomalous Nernst current induced by temperature gradient is described by  $J_c \propto E_{ANE} = -\alpha m \times \nabla T$ .<sup>35,37</sup> According to the classical Maxwell theory of electromagnetism, time-varying current will lead to the emission of electromagnetic waves, and the electric field is proportional to the time derivative of the current. Thus, the THz electric field induced by anomalous Nernst current could be described by  $E_{THz}(t) \propto \frac{\partial J_c(t)}{\partial t}$ , i.e., the THz emission is proportional to the ANE electric field  $E_{ANE}$ . To quantitatively analyze the dependence of the  $E_{ANE}$  on the thickness of the FM layer, we further calculated laser-induced temperature gradient in the FM layers in the case of substrate side pumping and film side pumping by ultrafast temperature simulation and adopted the values of the ANE coefficient  $\alpha$  from Ref. 35 to obtain  $E_{ANE}$ . As shown in Fig. 3(c), the simulation results are in satisfactory agreement with the experimental ones. This confirms again that the THz emission from FM film is dominated by ANE. In addition, the thickness of the FM layer and the incident direction of the laser can effectively modulate the magnitude and direction of the temperature gradient, thereby tuning the THz emissions.

### C. Interface and bulk anomalous Nernst effects

Based on a thorough analysis of the effect of  $t_{FM}$  on THz emission, it could be suggested that the temperature gradient may have two components associated with, respectively, the interface effect and the bulk effect.<sup>30,43</sup> Figures 4(a)–4(d) show the schematic diagrams of the laser-pulse-induced current originating from ANE for thin and thick FM layers when pumping different sample sides. Interfacial temperature gradient  $\nabla T_{int}$  establishes in the FM side near the NiFe/Al<sub>2</sub>O<sub>3</sub> interface, due to the thermal exchange between NiFe and Al<sub>2</sub>O<sub>3</sub>. It always points from substrate to FM layer, regardless of pumping side [Figs. 4(a) and 4(c)]. Notably, this interfacial effect is only dominant

when the FM layer is thin. With the increase in the FM layer thickness, the influence of the thermal exchange on temperature gradient is depressed, and the bulk effect gradually competes with the interface one. When the FM layer is thick enough, the bulk temperature gradient  $\nabla T_{bulk}$  becomes the major factor affecting ANE. It is worth pointing out that the direction of  $\nabla T_{bulk}$  is always against that of the incident laser pulse [Figs. 4(b) and 4(d)].

In this picture, the above experimental results can be qualitatively interpreted. When tuning THz emission by interface engineering,  $\nabla T_{int}$  will be significantly modified by buffer layer, resulting in a strong tuning to THz emission for thin FM layer samples since  $\nabla T_{int}$  plays a leading role now. In contrast, the effect of the buffer layer is unimportant when the FM layer is thick when  $\nabla T_{bulk}$  dominates the process of THz emission. Therefore, the tuning effect of the buffer layer exhibits the features of interfacial effects [Fig. 2(c)].

Next, we will analyze the dependence of THz emission on the thickness of the FM layer. When pumping substrate,  $\nabla T_{int}$  points from the substrate to FM layer [Fig. 4(a)] while  $\nabla T_{bulk}$  directs from the FM layer to substrate [Fig. 4(b)], resulting in oppositely directed transient currents. The competition of the interface and bulk effects leads to an evolution of the THz waveforms with the increase in  $t_{FM}$  and causes a polarity reversal when the FM layer is thick enough, as demonstrated by Figs. 3(b) and 3(c). Pumping film side, in contrast,  $\nabla T_{int}$  and  $\nabla T_{bulk}$  have the same direction along  $-z$  axis [Figs. 4(b) and 4(d)] and, therefore, the transient currents transport in the same direction. As a result, the THz waveforms from different FM layers have similar shapes [red curves in Fig. 2(a)]. In the picture of two component temperature gradient, we can also understand the variation of the THz polarity while flipping samples. Thin film flipping causes a direction reversal of  $\nabla T_{int}$ ; thus, a polarity reversal of THz waveforms [Figs. 4(a) and 4(c)]. In contrast, flipping a thick film does not change the direction of  $\nabla T_{bulk}$  [Figs. 4(b) and 4(d)]; thus, the THz polarity remains unaffected.

### D. THz emission of ferromagnetic metals with opposite anomalous Nernst coefficient

As discussed above, the THz pulse field  $E_{THz}$  induced by ANE has the form of  $E_{THz}(t) \propto E_{ANE} = -\alpha m \times \nabla T$ . According to this equation, the ANE coefficient  $\alpha$  is also a factor affecting THz polarity. To further confirm the relation between THz emission and ANE, we conducted experiments for samples with different FM films, including Fe, Co, and NiFe monolayers. THz waveforms of Al<sub>2</sub>O<sub>3</sub>/Fe(5 nm)/SiO<sub>2</sub>(3 nm), Al<sub>2</sub>O<sub>3</sub>/Co(5 nm)/SiO<sub>2</sub>(3 nm), and Al<sub>2</sub>O<sub>3</sub>/NiFe(5 nm)/SiO<sub>2</sub>(3 nm) samples are shown in Fig. 5(a), obtained by the pumping substrate. Notably, inspecting the relationship between THz polarity and the sign of the ANE/AHE coefficient of different FM films will provide a feasible way to distinguish the contributions from these two mechanisms to the THz emission of the FM monolayers.<sup>30</sup> Thus, further experimental measurements of ANE and AHE were performed on the above samples (see details in Sec. IV), and the results are shown in Figs. 5(b) and 5(c), respectively. We found that the sign of the ANE coefficient of the Fe film is opposite to that of the Co film, while the AHE coefficients of Fe and Co films have the same sign. Noting the simultaneous polarity change in the THz waveforms and the ANE coefficient from Fe to Co films, we can conclude that the THz emission is determined by ANE, rather than by AHE. In addition to this, the results of Co and NiFe films confirm this conclusion from an

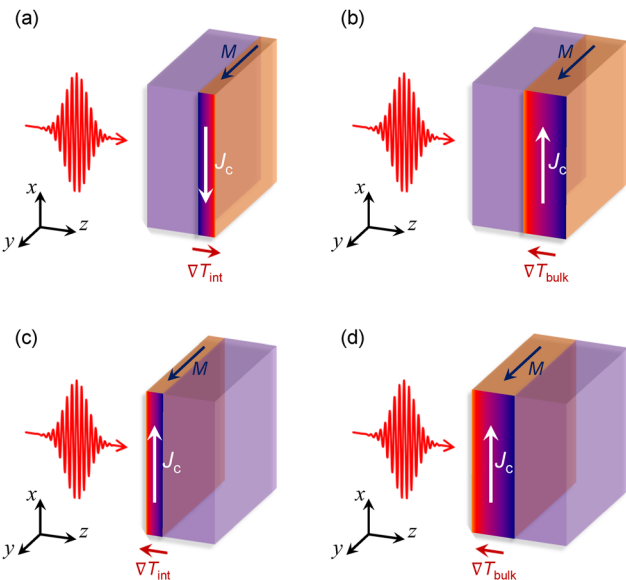


**FIG. 4.** (a) and (b) Schematic diagrams of the laser-induced thermally spin-polarized current originating from ANE for thin FM film (a) and thick FM film (b) for substrate side pumping. (c) and (d) The counterparts of (a) and (b) when the THz emission is excited by pumping film side.

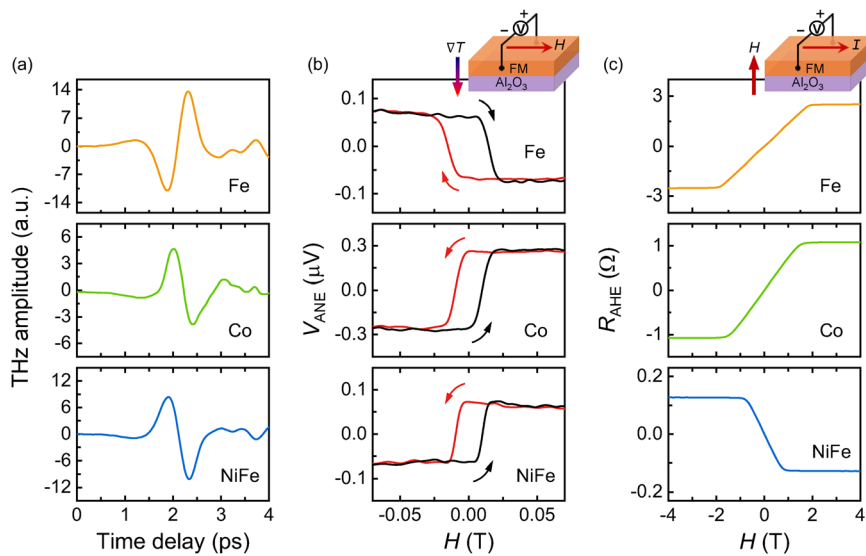


**FIG. 5.** (a) THz waveforms of  $Al_2O_3/Fe(5\text{ nm})/SiO_2(3\text{ nm})$ ,  $Al_2O_3/Co(5\text{ nm})/SiO_2(3\text{ nm})$ , and  $Al_2O_3/NiFe(5\text{ nm})/SiO_2(3\text{ nm})$  samples, obtained by pumping substrate. (b) Magnetic field dependence of the ANE voltage, measured under a fixed out-of-plane temperature gradient. Arrows in the figure mark the direction of magnetic cycling. The top inset is a schematic diagram of the ANE measurement. (c) Anomalous Hall resistance as a function of the magnetic field. The top inset is a schematic diagram of the AHE measurement.

alternative perspective. Notably, Co and NiFe films have the same THz polarity, which is consistent with the same sign of the ANE coefficient for Co and NiFe but contradicts the opposite sign of the AHE coefficient. Here, we would like to emphasize that these sign characteristics of the ANE and AHE coefficients for Fe, Co, and NiFe in our work are consistent with previously reported results.<sup>34,44,45</sup> Obviously, the THz polarity is strongly dependent on the sign of the ANE coefficient rather than the AHE coefficient. Therefore, comparing the THz polarity with the sign of ANE/AHE coefficient clearly demonstrates that ANE dominates THz emission in the FM monolayers, excluding the contributions from the AHE of hot electrons.

Moreover, we also found that the THz polarity of the 5-nm-thick Fe film reverses after inserting a  $SiO_2$  buffer layer, indicating that the tuning of the buffer layer to THz emission is ubiquitous for FM materials (Fig. S4). In addition, we also investigated THz radiation from 3-nm-thick NiFe samples with a  $SiO_2$  or a MgO buffer layer on different substrates, including  $SrTiO_3$  and  $KTaO_3$ , and THz polarity reversal is observed for all substrates (see Fig. S5 of the [supplementary material](#)). Obviously, introducing a buffer layer is a universal approach tuning the THz radiation of the FM metallic monolayers.

### III. CONCLUSION

We systematically investigate the THz emission from the NiFe layers on  $Al_2O_3$  substrates and verify the ANE mechanism for THz emission from a new perspective. The interface and bulk effects are the key ingredients for the ANE caused by the fs laser. The interface temperature gradient  $\nabla T_{int}$ , due to the thermal exchange between FM layer and substrate, can be effectively tuned by interface engineering. With the insertion of a  $SiO_2$  buffer layer between thin NiFe layers and  $Al_2O_3$ , an increase in intensity and a reversal in polarity are observed for the THz waveforms. This anomalous modulation is independent of the thickness of the buffer layer. Ultrafast temperature simulation indicates that the direction of  $\nabla T_{int}$  reverses after introducing a buffer layer. We further demonstrate the dependence of THz emission on the thickness of the NiFe layer without and with a buffer layer and found that the tuning effect of the buffer-layer is well consistent with

the features of interfacial effects. By analyzing the THz emission from different NiFe layers, we found that the thickness of the NiFe layer and the incident direction of the laser pulse effectively modify the magnitude and the direction of the temperature gradient. Moreover, the THz polarity reverses when the sign of ANE coefficient of the FM material is opposite. Therefore, the THz emission of a FM monolayer can be effectively modulated by tuning the magnetization direction, temperature gradient, and anomalous Nernst coefficient. This work demonstrates the importance of ultrafast spin caloritronics for the spintronic THz emitter.

## IV. METHODS

### A. Sample preparation

$Ni_{80}Fe_{20}$  (NiFe) and Fe films were grown on  $Al_2O_3$  substrates ( $10 \times 10 \times 0.5\text{ mm}^3$ ) by dc magnetron sputtering at room temperature.  $SrTiO_3$  and  $KTaO_3$  substrates were also used for comparison.  $SiO_2$  and MgO films were prepared at room temperature by radio frequency sputtering. The base pressure of the sputtering chamber was less than  $5 \times 10^{-5}\text{ Pa}$ . The sputtering was proceeded in an Ar atmosphere with a pressure of 0.35 Pa. Film thickness was determined by sputtering time, which has been carefully calibrated by small angle x-ray reflectivity. To prevent the NiFe or Fe film from oxidation, all samples were *in situ* capped with a 3-nm-thick  $SiO_2$  layer.

### B. THz emission spectroscopy

A standard THz time-domain spectroscopy setup was utilized to generate and detect the THz pulse waveforms. Linearly polarized femtosecond laser pulses from a commercial Ti:sapphire laser oscillator (central wavelength of 800 nm, pulse duration of 100 fs, repetition rate of 80 MHz) were focused onto the emission samples. To orient the magnetic moment of the FM layer, a magnetic field of 0.1 T was applied. The radiated THz pulses were captured by the electro-optic sampling method. All measurements were performed at room temperature in an environment of dry air to avoid disturbance by water vapor.



### C. Simulation model

The simulation of ultrafast temperature distributions and temperature gradients of the FM layer was carried out by using a one-dimensional two-temperature model (TTM).<sup>39</sup> This model treats the temporal and spatial evolution of electron and phonon temperatures separately and can describe the heat transfer path from electrons to substrates across the interface:

$$\begin{aligned} C_e \frac{\partial T_e}{\partial t} &= k_e \frac{\partial^2 T_e}{\partial z^2} - G(T_e - T_p) + S, \\ C_p \frac{\partial T_p}{\partial t} &= k_p \frac{\partial^2 T_p}{\partial z^2} + G(T_e - T_p), \\ C_{s_1} \frac{\partial T_{s_1}}{\partial t} &= k_{s_1} \frac{\partial^2 T_{s_1}}{\partial z^2}, \\ C_{s_2} \frac{\partial T_{s_2}}{\partial t} &= k_{s_2} \frac{\partial^2 T_{s_2}}{\partial z^2}, \end{aligned}$$

with the interface conditions:

$$\begin{aligned} q_e|_{z=0} &= -\frac{T_e - T_{s_1}}{R_{es_1}} \Big|_{z=0}, & q_e|_{z=L} &= -\frac{T_{s_2} - T_e}{R_{es_2}} \Big|_{z=L}, \\ q_p|_{z=0} &= -\frac{T_p - T_{s_1}}{R_{ps_1}} \Big|_{z=0}, & q_p|_{z=L} &= -\frac{T_{s_2} - T_p}{R_{ps_2}} \Big|_{z=L}, \\ q_{s_1}|_{z=-L_1} &= 0, & q_{s_1}|_{z=0} &= -\frac{T_e - T_{s_1}}{R_{es_1}} \Big|_{z=L} - \frac{T_p - T_{s_1}}{R_{ps_1}} \Big|_{z=L}, \\ q_{s_2}|_{z=L} &= -\frac{T_{s_2} - T_e}{R_{es_2}} \Big|_{z=L} - \frac{T_{s_2} - T_p}{R_{ps_2}} \Big|_{z=L}, & q_{s_2}|_{z=L+L_2} &= 0. \end{aligned}$$

The subscripts e and p represent electrons and phonons in the Ni film, respectively. The subscript  $s_1$  represents the  $\text{Al}_2\text{O}_3$  substrate ( $\text{SiO}_2$  buffer layer) for the unbuffered (buffered) sample, and subscript  $s_2$  represents the  $\text{SiO}_2$  capping layer.  $T$ ,  $C$ ,  $k$ ,  $G$ , and  $S$  are the temperature, the volumetric specific heat capacity, the thermal conductivity, the electron–phonon coupling factor, and the heat source, respectively. In the interface conditions,  $q$  and  $R$  are the heat flux and the interface thermal resistance at every interfaces.  $L$ ,  $L_1$ , and  $L_2$  are thicknesses of the Ni film, the  $\text{Al}_2\text{O}_3$  substrate ( $\text{SiO}_2$  buffer layer) for the unbuffered (buffered) sample, and the  $\text{SiO}_2$  capping layer.

The laser source term  $S$  is given as

$$S = 0.94 \frac{(1 - Re - Tr)F}{\delta t_p [1 - \exp(-\frac{L_{\text{Ni}}}{\delta})]} \exp \left[ -\frac{d}{\delta} - 2.77 \left( \frac{t}{t_p} \right)^2 \right].$$

This equation assumes a temporal Gaussian pulse with the full width at half maximum  $t_p$  and the optical absorption of Ni film with the absorption depth  $Re$  and  $Tr$  are reflectance and transmission, respectively, calculated by transfer matrix toward multilayer samples.  $F$  is the fluence of laser.  $t_{\text{Ni}}$  is the thickness of the Ni film.  $d$  is the distance between the spatial position and the Ni surface irradiated by the laser.

The thermophysical parameters used in the simulation are listed in Table I. Note that the electron specific heat capacity and thermal conductivity of Ni are obtained via polynomial fitting for the simulation results in Ref. 46 involving the density of states (DOS), and the expressions are as follows:

$$\begin{aligned} C_e(T_e) &= 110930.665 + 1164.9 \times T_e \\ &\quad - 1.8186 \times T_e^2 + 1.58 \times 10^{-3} \times T_e^3 \\ &\quad - 6.268 \times 10^{-7} \times T_e^4 + 9.3748 \times 10^{-11} \times T_e^5, \\ k_e(T_e) &= 60.7049 + 0.1589 \times T_e - 1.7497 \times 10^{-4} \times T_e^2 \\ &\quad + 1.3329 \times 10^{-7} \times T_e^3 - 4.2228 \times 10^{-11} \times T_e^4 \\ &\quad + 4.7956 \times 10^{-15} \times T_e^5. \end{aligned}$$

### D. ANE and AHE measurements

The anomalous Nernst effect (ANE) and anomalous Hall effect (AHE) of different FM monolayers, including Fe, Co, and NiFe, were measured by a quantum-designed physical property measurement system (PPMS) at room temperature. To generate a thermally spin-polarized current by the ANE, we employ the longitudinal experimental setup with a uniform out-of-plane temperature gradient ( $\nabla T$ ), as shown in the top inset of Fig. 5(b). The temperature gradient is measured with thermocouples. To reduce systematic errors, we used a constant heating power instead of a constant temperature difference to conduct the measurement (see details in Ref. 49). An external in-plane magnetic field ( $H$ ) is used to align the magnetization of all FM monolayers, and the ANE voltage ( $V_{\text{ANE}}$ ) is measured along the direction perpendicular to  $H$ . The magnetic field dependence of  $V_{\text{ANE}}$  is measured under a fixed temperature gradient of  $\nabla T \approx 18.8 \text{ K/cm}$  (corresponding to a heating power of  $P = 65 \text{ mW}$ ). The van der Pauw geometry was adopted for AHE measurements with an applied current

TABLE I. Summary of the thermophysical parameters in the TTM.

Parameter (units)	Value	Parameter (units)	Value
$C_e$ ( $\text{J}\cdot\text{m}^{-3}\cdot\text{K}^{-1}$ ) (Ref. 46)	$C_e(T_e)$	$k_e$ ( $\text{W}\cdot\text{m}^{-1}\cdot\text{K}^{-1}$ ) (Ref. 46)	$k_e(T_e)$
$C_p$ ( $\text{J}\cdot\text{m}^{-3}\cdot\text{K}^{-1}$ ) (Ref. 47)	$3.94 \times 10^6$	$k_p$ ( $\text{W}\cdot\text{m}^{-1}\cdot\text{K}^{-1}$ ) (Ref. 47)	9.6
$C_{s_1}$ ( $\text{J}\cdot\text{m}^{-3}\cdot\text{K}^{-1}$ ) (Refs. 41 and 42)	$3.06 \times 10^6$ for $\text{Al}_2\text{O}_3/1.92 \times 10^6$ for $\text{SiO}_2$	$k_{s_1}$ ( $\text{W}\cdot\text{m}^{-1}\cdot\text{K}^{-1}$ ) (Refs. 41 and 42)	36.96 for $\text{Al}_2\text{O}_3/1.34$ for $\text{SiO}_2$
$C_{s_2}$ ( $\text{J}\cdot\text{m}^{-3}\cdot\text{K}^{-1}$ ) (Ref. 41)	$1.92 \times 10^6$	$k_{s_2}$ ( $\text{W}\cdot\text{m}^{-1}\cdot\text{K}^{-1}$ ) (Ref. 41)	1.34
$R_{es_1}$ ( $\text{K}\cdot\text{m}^2\cdot\text{W}^{-1}$ )	$1 \times 10^{-8}$	$R_{ps_1}$ ( $\text{K}\cdot\text{m}^2\cdot\text{W}^{-1}$ )	$10^{-7}$
$R_{es_2}$ ( $\text{K}\cdot\text{m}^2\cdot\text{W}^{-1}$ )	$2 \times 10^{-10}$	$R_{ps_2}$ ( $\text{K}\cdot\text{m}^2\cdot\text{W}^{-1}$ )	$10^{-7}$
$\delta$ (nm) (Ref. 48)	13	$G$ ( $\text{W}\cdot\text{m}^{-3}\cdot\text{K}^{-1}$ ) (Ref. 46)	$8 \times 10^{17}$
$F$ ( $\text{J}\cdot\text{m}^{-2}$ )	0.7	$t_p$ (fs)	100

of 1 mA. Ultrasonic wire bonding (Al wire of 20  $\mu\text{m}$  diameter) was used for electrode contact.

### SUPPLEMENTARY MATERIAL

See the [supplementary material](#) for detail on the calculation of the THz electric field from the temperature gradient, THz emissions of  $\text{Al}_2\text{O}_3/\text{NiFe}(5\text{ nm})/\text{SiO}_2(3\text{ nm})$  and  $\text{Al}_2\text{O}_3/\text{SiO}_2(3\text{ nm})/\text{NiFe}(5\text{ nm})/\text{SiO}_2(3\text{ nm})$  under opposite magnetic field directions, two-dimensional color maps of phonon temperature distribution in  $\text{Al}_2\text{O}_3/\text{Ni}(5\text{ nm})/\text{SiO}_2(3\text{ nm})$  and  $\text{Al}_2\text{O}_3/\text{SiO}_2(3\text{ nm})/\text{Ni}(5\text{ nm})/\text{SiO}_2(3\text{ nm})$ , work steps for the extraction of the THz electric field from the calculated temperature gradient, THz emissions of the 5-nm-thick Fe film without and with the  $\text{SiO}_2$  buffer layer, THz emissions of the 3-nm-thick NiFe samples with buffer layer on different substrates.

### ACKNOWLEDGMENTS

This work has been supported by the Science Center of the National Science Foundation of China (Grant No. 52088101), the National Key Research and Development Program of China (Grant Nos. 2022YFA1403302, 2019YFA0704904, 2020YFA0711502, 2021YFA1401400, 2021YFB3501202, 2021YFA1400300, and 2022YFB3505201), the National Natural Science Foundation of China (Grant Nos. 11934016, 51972335, 12004022, 62027807, 62005256, 52176075, 11921004, 11934016, 12104027, 12104029, 92263202, and 12274443), the Strategic Priority Research Program B (Grant No. XDB33030200), the Key Research Programs (Grant No. ZDRW-CN-2021-3) of the Chinese Academy of Sciences, the open research fund of Songshan Lake Materials Laboratory (Grant No. 2022SLABFN23), and the University Consistent Support Program of Shenzhen Natural Science Foundation (Grant No. 20200925155828001). J.R.S. is thankful for the support of the Project for Innovative Research Team of National Natural Science Foundation of China (Grant No. 11921004).

### AUTHOR DECLARATIONS

#### Conflict of Interest

The authors have no conflicts to disclose.

#### Author Contributions

**Hui Zhang:** Data curation (lead); Funding acquisition (equal); Investigation (lead); Project administration (lead); Writing – original draft (lead); Writing – review & editing (lead). **Furong Han:** Investigation (supporting). **Huaiwen Yang:** Investigation (supporting). **Wei Tan:** Investigation (supporting). **Yuansha Chen:** Investigation (supporting). **Feng-xia Hu:** Investigation (supporting). **Jian-Wang Cai:** Investigation (equal). **Liang Guo:** Investigation (equal); Software (lead); Writing – review & editing (equal). **Sunmi Shin:** Writing – review & editing (supporting). **Weisheng Zhao:** Investigation (equal). **B. G. Shen:** Investigation (equal). **Zheng Feng:** Data curation (lead); Investigation (lead); Writing – original draft (equal); Writing – review & editing (equal). **Jirong Sun:** Funding acquisition (lead); Investigation (lead); Project administration (lead); Writing – original draft (lead); Writing – review & editing (lead). **Guansong Li:** Investigation (equal). **Liang Zhang:** Investigation (equal); Software (lead); Writing – original draft (supporting).

**Xiaobing Chen:** Investigation (equal); Software (equal). **He Bai:** Investigation (supporting). **Song Sun:** Software (supporting). **Jin Tang:** Software (supporting). **Jine Zhang:** Investigation (supporting).

### DATA AVAILABILITY

The data that support the findings of this study are available within the article and its [supplementary material](#).

### REFERENCES

- <sup>1</sup>T. Kampfrath, M. Battiato, P. Maldonado, G. Eilers, J. Noetzdold, S. Maehrlin, V. Zbarsky, F. Freimuth, Y. Mokrousov, S. Bluegel, M. Wolf, I. Radu, P. M. Oppeneer, and M. Muenzenberg, *Nat. Nanotechnol.* **8**, 256 (2013).
- <sup>2</sup>T. Seifert, S. Jaiswal, U. Martens, J. Hannegan, L. Braun, P. Maldonado, F. Freimuth, A. Kronenberg, J. Henzli, I. Radu, E. Beaurepaire, Y. Mokrousov, P. M. Oppeneer, M. Jourdan, G. Jakob, D. Turchinovich, L. M. Hayden, M. Wolf, M. Muenzenberg, M. Klaui, and T. Kampfrath, *Nat. Photonics* **10**, 483 (2016).
- <sup>3</sup>Y. Wu, M. Elyasi, X. Qiu, M. Chen, Y. Liu, L. Ke, and H. Yang, *Adv. Mater.* **29**, 1603031 (2017).
- <sup>4</sup>Z. Feng, R. Yu, Y. Zhou, H. Lu, W. Tan, H. Deng, Q. Liu, Z. Zhai, L. Zhu, J. Cai, B. Miao, and H. Ding, *Adv. Opt. Mater.* **6**, 1800965 (2018).
- <sup>5</sup>D. Yang, J. Liang, C. Zhou, L. Sun, R. Zheng, S. Luo, Y. Wu, and J. Qi, *Adv. Opt. Mater.* **4**, 1944 (2016).
- <sup>6</sup>M. B. Jungfleisch, Q. Zhang, W. Zhang, J. E. Pearson, R. D. Schaller, H. Wen, and A. Hoffmann, *Phys. Rev. Lett.* **120**, 207207 (2018).
- <sup>7</sup>C. Zhou, Y. P. Liu, Z. Wang, S. J. Ma, M. W. Jia, R. Q. Wu, L. Zhou, W. Zhang, M. K. Liu, Y. Z. Wu, and J. Qi, *Phys. Rev. Lett.* **121**, 086801 (2018).
- <sup>8</sup>E. Beaurepaire, G. M. Turner, S. M. Harrel, M. C. Beard, J. Y. Bigot, and C. A. Schmuttenmaer, *Appl. Phys. Lett.* **84**, 3465 (2004).
- <sup>9</sup>C. A. Meserole, G. L. Fisher, D. J. Hilton, R. D. Averitt, D. J. Funk, and A. J. Taylor, *Appl. Surf. Sci.* **253**, 6992 (2007).
- <sup>10</sup>S. Jian, H. W. Zhang, and Y. X. Li, *Chin. Phys. Lett.* **29**, 067502 (2012).
- <sup>11</sup>N. Kumar, R. W. A. Hendrikx, A. J. L. Adam, and P. C. M. Planken, *Opt. Express* **23**, 14252 (2015).
- <sup>12</sup>M. Venkatesh, S. Ramakanth, A. K. Chaudhary, and K. C. J. Raju, *Opt. Mater. Express* **6**, 2342 (2016).
- <sup>13</sup>S. Zhang, Z. Jin, X. Liu, W. Zhao, X. Lin, C. Jing, and G. Ma, *Opt. Lett.* **42**, 3080 (2017).
- <sup>14</sup>L. Cheng, X. Wang, W. Yang, J. Chai, M. Yang, M. Chen, Y. Wu, X. Chen, D. Chi, K. E. J. Goh, J. X. Zhu, H. Sun, S. Wang, J. C. W. Song, M. Battiato, H. Yang, and E. E. M. Chia, *Nat. Phys.* **15**, 347 (2019).
- <sup>15</sup>T. J. Huisman, R. V. Mikhaylovskiy, A. Tsukamoto, T. Rasing, and A. V. Kimel, *Phys. Rev. B* **92**, 104419 (2015).
- <sup>16</sup>L. Huang, J. W. Kim, S. H. Lee, S. D. Kim, V. M. Tien, K. P. Shinde, J. H. Shim, Y. Shin, H. J. Shin, S. Kim, J. Park, S. Y. Park, Y. S. Choi, H. J. Kim, J. I. Hong, D. E. Kim, and D. H. Kim, *Appl. Phys. Lett.* **115**, 142404 (2019).
- <sup>17</sup>W. Zhang, P. Maldonado, Z. Jin, T. S. Seifert, J. Arabski, G. Schmerber, E. Beaurepaire, M. Bonn, T. Kampfrath, P. M. Oppeneer, and D. Turchinovich, *Nat. Commun.* **11**, 4247 (2020).
- <sup>18</sup>K. Lee, D. K. Lee, D. Yang, R. Mishra, D. J. Kim, S. Liu, Q. Xiong, S. K. Kim, K. J. Lee, and H. Yang, *Nat. Nanotechnol.* **16**, 1337 (2021).
- <sup>19</sup>G. Li, R. Medapalli, J. H. Mentink, R. V. Mikhaylovskiy, T. G. H. Blank, S. K. K. Patel, A. K. Zvezdin, T. Rasing, E. E. Fullerton, and A. V. Kimel, *Nat. Commun.* **13**, 2998 (2022).
- <sup>20</sup>L. Huang, S. H. Lee, S. D. Kim, J. H. Shim, H. J. Shin, S. Kim, J. Park, S. Y. Park, Y. S. Choi, H. J. Kim, J. I. Hong, D. E. Kim, and D. H. Kim, *Sci. Rep.* **10**, 15843 (2020).
- <sup>21</sup>Beaurepaire, Merle and Daunois, Bigot, *Phys. Rev. Lett.* **76**, 4250 (1996).
- <sup>22</sup>J. Y. Bigot, M. Vomer, and E. Beaurepaire, *Nat. Phys.* **5**, 515 (2009).
- <sup>23</sup>B. Koopmans, G. Malinowski, F. Dalla Longa, D. Steiauf, M. Faehnl, T. Roth, M. Cinchetti, and M. Aeschlimann, *Nat. Mater.* **9**, 259 (2010).
- <sup>24</sup>J. Tang, Y. J. Ke, W. He, X. Q. Zhang, W. Zhang, N. Li, Y. S. Zhang, Y. Li, and Z. H. Cheng, *Adv. Mater.* **30**, 1706439 (2018).
- <sup>25</sup>K. Neeraj, N. Awari, S. Kovalev, D. Polley, N. Zhou Hagstrom, S. S. P. K. Arekapudi, A. Semisalova, K. Lenz, B. Green, J. C. Deinert, I. Ilyakov, M. Chen,

- M. Bawatna, V. Scalera, M. D'Aquino, C. Serpico, O. Hellwig, J. E. Wegrowe, M. Gensch, and S. Bonetti, *Nat. Phys.* **17**, 245 (2021).
- <sup>26</sup>Q. Zhang, Z. Luo, H. Li, Y. Yang, X. Zhang, and Y. Wu, *Phys. Rev. Appl.* **12**, 054027 (2019).
- <sup>27</sup>Y. Liu, H. Cheng, Y. Xu, P. Vallobra, S. Eimer, X. Zhang, X. Wu, T. Nie, and W. Zhao, *Phys. Rev. B* **104**, 064419 (2021).
- <sup>28</sup>T. S. Seifert, S. Jaiswal, J. Barker, S. T. Weber, I. Rzdolski, J. Cramer, O. Gueckstock, S. F. Maehrlein, L. Nadvornik, S. Watanabe, C. Ciccarelli, A. Melnikov, G. Jakob, M. Muenzenberg, S. T. B. Goennenwein, G. Woltersdorf, B. Rethfeld, P. W. Brouwer, M. Wolf, M. Klauui, and T. Kampfrath, *Nat. Commun.* **9**, 2899 (2018).
- <sup>29</sup>W. Lu, Z. Fan, Y. Yang, J. Ma, J. Lai, X. Song, X. Zhuo, Z. Xu, J. Liu, X. Hu, S. Zhou, F. Xiu, J. Cheng, and D. Sun, *Nat. Commun.* **13**, 1623 (2022).
- <sup>30</sup>Z. Feng, W. Tan, Z. Jin, Y. J. Chen, Z. F. Zhong, L. Zhang, S. Sun, J. Tang, Y. X. Jiang, P. H. Wu, J. Cheng, B. F. Miao, H. F. Ding, D. C. Wang, Y. M. Zhu, L. Guo, S. Shin, G. H. Ma, D. Z. Hou, and S. Y. Huang, *arXiv:2302.11134*.
- <sup>31</sup>S. Y. Huang, W. G. Wang, S. F. Lee, J. Kwo, and C. L. Chien, *Phys. Rev. Lett.* **107**, 216604 (2011).
- <sup>32</sup>Y. Sakuraba, K. Hasegawa, M. Mizuguchi, T. Kubota, S. Mizukami, T. Miyazaki, and K. Takanashi, *Appl. Phys. Express* **6**, 033003 (2013).
- <sup>33</sup>K. D. Lee, D. J. Kim, H. Y. Lee, S. H. Kim, J. H. Lee, K. M. Lee, J. R. Jeong, K. S. Lee, H. S. Song, J. W. Sohn, S. C. Shin, and B. G. Park, *Sci. Rep.* **5**, 10249 (2015).
- <sup>34</sup>H. Kannan, X. Fan, H. Celik, X. Han, and J. Q. Xiao, *Sci. Rep.* **7**, 6175 (2017).
- <sup>35</sup>T. C. Chuang, P. L. Su, P. H. Wu, and S. Y. Huang, *Phys. Rev. B* **96**, 174406 (2017).
- <sup>36</sup>K. Uchida, S. Takahashi, K. Harii, J. Ieda, W. Koshibae, K. Ando, S. Maekawa, and E. Saitoh, *Nature* **455**, 778 (2008).
- <sup>37</sup>K. Hasegawa, M. Mizuguchi, Y. Sakuraba, T. Kamada, T. Kojima, T. Kubota, S. Mizukami, T. Miyazaki, and K. Takanashi, *Appl. Phys. Lett.* **106**, 252405 (2015).
- <sup>38</sup>J. Lombard, F. Detcheverry, and S. Merabia, *J. Phys.* **27**, 015007 (2015).
- <sup>39</sup>L. Guo, S. L. Hodson, T. S. Fisher, and X. Xu, *J. Heat Transfer* **134**, 042402 (2012).
- <sup>40</sup>Q. Yao, L. Guo, V. Iyer, and X. Xu, *Heat Transfer Eng.* **40**, 1211 (2019).
- <sup>41</sup>S. Andersson and L. Dzhavadov, *J. Phys.* **4**, 6209 (1992).
- <sup>42</sup>Y. S. Touloukian, *Thermophysical Properties of High Temperature Solid Materials. Vol. 4. Oxides and Their Solutions and Mixtures* (MacMillan, New York, 1967).
- <sup>43</sup>Y. J. Chen and S. Y. Huang, *Phys. Rev. B* **99**, 094426 (2019).
- <sup>44</sup>L. Ma, Y. Zhang, H. Zhao, H. R. Fu, M. Tang, H. L. Yang, Z. Shi, N. Tian, and C. Y. You, *AIP Adv.* **9**, 035227 (2019).
- <sup>45</sup>X. Wang, D. Vanderbilt, J. R. Yates, and I. Souza, *Phys. Rev. B* **76**, 195109 (2007).
- <sup>46</sup>Z. Lin and L. V. Zhigilei, *Appl. Surf. Sci.* **253**, 6295 (2007).
- <sup>47</sup>J. E. Pudell, M. Mattern, M. Hehn, G. Malinowski, M. Herzog, and M. Bargheer, *Adv. Funct. Mater.* **30**, 2004555 (2020).
- <sup>48</sup>P. B. Johnson and R. W. Christy, *Phys. Rev. B* **9**, 5056 (1974).
- <sup>49</sup>H. R. Zhang, Y. Ma, H. Zhang, X. B. Chen, S. H. Wang, G. Li, Y. Yun, X. Yan, Y. S. Chen, F. X. Hu, J. W. Cai, B. G. Shen, W. Han, and J. R. Sun, *Nano Lett.* **19**, 1605 (2019).